JPhys Materials

PAPER • OPEN ACCESS

Constructing defect-rich $Ni_9S_8/Fe_5Ni_4S_8$ heterostructure nanoparticles for efficient oxygen evolution reaction and overall water splitting

To cite this article: Jinxiao Xu *et al* 2021 *J. Phys. Mater.* **4** 034006

Journal of Physics: Materials

PAPER

Constructing defect-rich $Ni_9S_8/Fe_5Ni_4S_8$ heterostructure nanoparticles for efficient oxygen evolution reaction and overall water splitting

Jinxiao Xu[1], **Yingjun Ma**[1], **Jie Wang**[1], **Xuyun Guo**[2], **Linghao Su**[1], **Chuanli Ma**[1], **Liangyu Gong**[1], **Ye Zhu**[2] and **Cuijuan Xuan**[1,*]

[1] College of Chemistry and Pharmaceutical Sciences, Qingdao Agricultural University, Qingdao 266109, People's Republic of China
[2] Department of Applied Physics, The Hong Kong Polytechnic University, Hung Horn, Kowloon, Hong Kong, People's Republic of China
* Author to whom any correspondence should be addressed.

E-mail: cjxuan@qau.edu.cn

Keywords: oxygen evolution reaction, Ni–Fe sulfide, heterostructured nanoparticle, electrochemical water splitting

Supplementary material for this article is available online

OPEN ACCESS

RECEIVED
31 December 2020

REVISED
8 March 2021

ACCEPTED FOR PUBLICATION
30 March 2021

PUBLISHED
21 April 2021

Abstract

Designing electrocatalysts from the perspective of modulating electronic structure and morphology has received considerable research interest in enhancing the electrocatalytic performance for oxygen evolution reaction (OER). In this work, nickel–iron based sulfides were synthesized through a one-pot hydrothermal approach which is characterized as defect-rich $Ni_9S_8/Fe_5Ni_4S_8$ heterostructured nanoparticles. The presence of two phases, numerous defects, and uniformly distributed nanoparticles with the porous structure are conducive to modulating electronic structure, facilitating electron and mass transport, allowing the effective accessibility of active sites. The as-prepared $Ni_9S_8/Fe_5Ni_4S_8$ exhibits enhanced electrocatalytic OER activity and long-lasting stability, which needs an overpotential of 239 mV for yielding 10 mA cm^{-2} and long-term stability better than RuO_2. Furthermore, when employed in a two-electrode overall water splitting system, the catalyst coupled with Pt/C configuration exhibits comparable electrocatalytic performance to Pt/C and RuO_2 based electrolyzer. This work not only offers a highly efficient and promising candidate catalyst for electrocatalytic water oxidation but also provides a simple synthesis method to heterostructured nanoparticles for other energy-related applications.

1. Introduction

Developing the renewable and sustainable energy system is of vital significance to address the current energy and environmental issues due to the extensive use of fossil fuels. Photocatalytic water splitting and electrochemical water splitting are two important technologies for producing renewable hydrogen [1–6]. The energy consumption of water electrolysis is largely limited by the sluggish kinetics of anodic oxygen evolution reaction (OER). Therefore, developing highly efficient electrocatalysts towards OER presents a crucial challenge and has become a research spot in the production of hydrogen by electrochemical water splitting [7, 8]. Currently, Ru or Ir based precious-metal materials are considered to possess high OER activity whereas their widespread utilization is largely impeded by the scarcity, costliness, and inferior long-lasting abilities [9], which promotes us to look for highly efficient and cost-effective alternatives on the basis of earth-abundant elements. To the end, numerous researches have concentrated on exploring 3d transition-metal (TM) based electrocatalysts especially Fe, Co, Ni-based materials due to their earth abundance, low price, and relatively competitive OER activity [10–12].

Among various TM-based catalysts, Ni and Fe based oxides/hydroxides are demonstrated to show excellent catalytic performance thanks to the synergistic effect of nickel and iron [13–16]. For example, Xiao *et al* [17] reported that iron and nickel of (Ni,Fe)OOH catalysts can promote the generation of an active O

radical intermediate and catalyze O–O coupling, respectively, reflecting the synergy between Fe and Ni favorable for enhancing the OER activity. Considering the poor intrinsic conductivity of oxides/hydroxides, various approaches have been proposed to facilitate the electrocatalytic activity such as exploring non-oxide materials (e.g. sulfides, phosphides, selenides) [18–21], and introducing conductive substrate [22]. Compared with oxide, TM-based sulfides have attracted tremendous attention due to the better electronic conductivity and the different valence of metal [23–25]. For instance, Wang *et al* [26] synthesized $FeNi_2S_4$ hollow balloons by a template-free solvothermal approach to acquire 10 mA cm^{-2} at an overpotential of 273 mV. Ni *et al* [27] prepared $(NiFe)S_2$ pyrite mesocrystals with nearly single crystalline porous cubes which delivered 10 mA cm^{-2} at overpotential of 260 mV. On the other hand, constructing heterostructure is deemed as another efficient tactics to promote the electrocatalytic activity by integrating different component properties [28, 29]. Besides, the defect and interface generated by heterostructure could optimize the absorption energy of reactant, intermediate, and product [30–33]. Du *et al* [29] prepared a defect-rich Co_9S_8/Ni_3S_2 heterostructure which could regulate the local electronic arrangement and optimize the chemisorption of reactants, leading to the performance improvement of electrochemical water splitting. Given the above mentioned, it is highly desirable but still challenging to construct defect-rich Ni and Fe based heterostructure with excellent water oxidation activity.

Herein, we present a simply one-pot hydrothermal approach to prepare a heterostructured hybrid material, composed of $Ni_9S_8/Fe_5Ni_4S_8$ heterostructural nanoparticles featuring rich defects. The unique composition and structure of $Ni_9S_8/Fe_5Ni_4S_8$ are favorable for optimizing the electronic structure and adsorption of intermediates, and these advantages making $Ni_9S_8/Fe_5Ni_4S_8$ exhibiting superior electrocatalytic activity and stability. When used in overall water splitting, $Ni_9S_8/Fe_5Ni_4S_8$ also possesses excellent electrocatalytic performance.

2. Experimental methods

2.1. Preparation of nickel and iron based sulfides

Ni–Fe based sulfides (Ni–Fe–S) were prepared through a one-pot hydrothermal approach. Typically, 1.5 mmol of $NiCl_2 \cdot 6H_2O$ (99.9%), 0.3 mmol of $FeCl_2 \cdot 4H_2O$ (99.0%), and 9 mmol of hexamethylenetetramine (HMT, ⩾99.0%) were dissolved in 60 ml of mixed solution (30 ml N,N-dimethylformamide + 30 ml ethylene glycol) under stirring to form a clear solution. After that, 8 mmol thioacetamide (TAA, ⩾99.0%) was added to the solution following by hydrothermal treatment at 200 °C for 18 h. The precipitate was obtained through centrifugation and washed with ethanol and water several times before lyophilization. The resulting product was represented by Ni–Fe–S(5:1), in which 5:1 represents the molar ratio of Ni and Fe precursors. For comparison, other Ni–Fe sulfides were also synthesized based on the same preparation procedure except changing the adding amount of Ni and Fe precursors or the hydrothermal temperature. Besides, Ni–Fe–O, Ni–S, Fe–S materials were prepared in a similar approach as Ni–Fe–S(5:1) except not adding TAA, $FeCl_2 \cdot 4H_2O$, or $NiCl_2 \cdot 6H_2O$.

2.2. Physical characterization

Scanning electron microscopy (SEM), and transmission electron microscopy (TEM) images were obtained on JSM-7500F and JSM-2100F equipment, respectively. The crystal structure and surface information were obtained by using X'Pert PRO diffractometer (Bruker D8) and AXIS-ULTRA DLD Instrument to carrying out powder x-ray diffraction (XRD) and x-ray photoelectron spectroscopy (XPS), respectively. IRIS advantage spectrometer (Thermo Elemental Co., USA) was used to perform inductively coupled plasma atomic emission spectroscopy (ICP-AES).

2.3. Electrochemical measurement

Electrocatalytic properties of the materials were determined in 1.0 M KOH using the CHI 760e instrument at ambient temperature. A three-electrode configuration was employed with a reversible hydrogen electrode, a carbon rod, and a rotating-disk glassy carbon electrode (GCE), as the reference electrode, counter electrode, and working electrode, respectively. To obtain the working electrode, 5.0 mg of catalysts was mixed with 1.0 ml of Nafion/isopropyl alcohol solution under sonication, and the resulting homogeneous suspension (16.5 μl) was dropped onto GCE and then dried at room temperature. Cyclic voltammetry (CV) and linear sweep voltammetry (LSV) curves were acquired at a rotation speed of 1600 rpm and a scan rate of 5 mV s^{-1}. Electrochemical impedance spectroscopy (EIS) was performed at the potential of 1.5 V in the frequency from 100 kHz to 0.01 Hz.

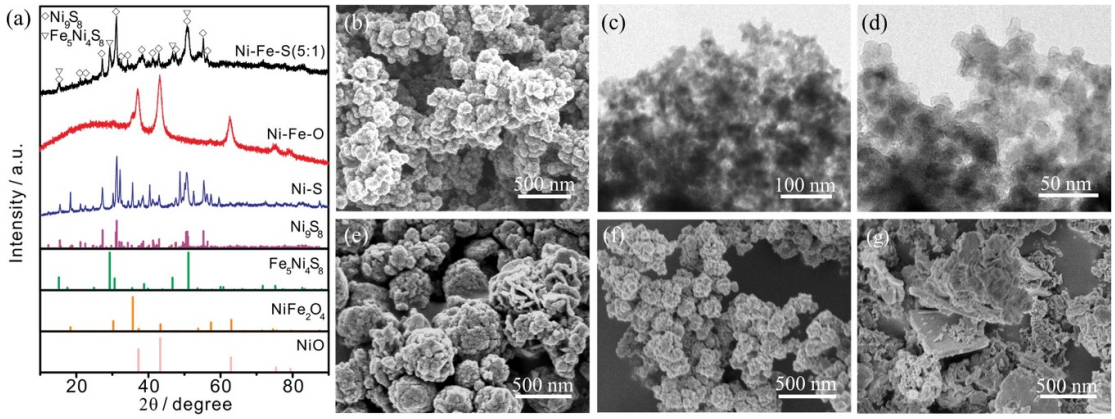

Figure 1. (a) XRD patterns of Ni–Fe–O, Ni–S, and Ni–Fe–S(5:1) materials. (b) SEM and (c), (d) TEM images of Ni–Fe–S(5:1). SEM images of (e) Ni–Fe–O, (f) Ni–S, (g) Fe–S.

3. Results and discussion

The Ni–Fe sulfide was prepared through a simple one-pot hydrothermal strategy with $NiCl_2 \cdot 6H_2O$, $FeCl_2 \cdot 4H_2O$, HMT, and TAA as precursors. The contrast materials were also obtained by simply controlling the addition of precursors. The crystal structure of the materials was demonstrated by XRD patterns (figure 1). For Ni–Fe–S(5:1), the peaks at 15.50°, 21.22°, 22.54°, 27.35°, 31.27°, 31.99°, 32.63°, 34.37°, 41.35°, 43.02°, 47.74°, 50.85°, 55.35°, and 56.45° are indexed to (111), (201), (112), (131), (311), (132), (023), (203), (150), (421), (333), (440), (404), and (262) planes of Ni_9S_8 (JCPDS card 078-1886), and the peaks at 15.19°, 29.32°, 38.86°, 46.73°, and 51.15° correspond to (111), (311), (331), (511), and (440) planes of $Fe_5Ni_4S_8$ (JCPDS card 086-2470). Obviously, the XRD results of Ni–Fe–S(5:1) illustrate the successful formation of sulfides with two different phases. For comparison, Ni–Fe–O and Ni–S were prepared without adding TAA or Fe precursors. The corresponding XRD patterns show that Ni–Fe–O displays typical diffraction patterns of NiO (JCPDS card 065-5745) and $NiFe_2O_4$ (JCPDS card 089-4927). The XRD pattern of Ni–S is mainly indexed to Ni_9S_8 with a small amount of NiS (JCPDS card 086-2281).

The morphology of the materials was examined by SEM and TEM images. It is found in figure 1(b) that Ni–Fe–S(5:1) is composed of numerous nanoparticles and figures 1(c) and (d) further show the uniform distribution of nanoparticles. Besides, the formation of porous structures was displayed clearly in figures 1(c) and (d), which is favorable for the full contact between materials and electrolyte during electrocatalytic process and the better utilization of active sites. The particle size distribution in figure S1 (available online at stacks.iop.org/JPMATER/4/034006/mmedia) demonstrates most of the nanoparticle diameter is in the range of 12 and 20 nm. In contrast, SEM images depicted in figure 1(e) show the nanosphere structure of Ni–Fe–O, the particle of which is much larger than Ni–Fe sulfides obtained at the Ni and Fe molar ratio of 5:1, suggesting the particles are more likely to aggregate in the absence of sulfur source during hydrothermal treatment. In the absence of Ni or Fe precursors, the obtained Ni–S displays uniformly distributed nanoparticle structure (figure 1(f)), while the resulting Fe–S shows two structures of nanoparticles and nanoplates (figure 1(g)). STEM, high-resolution TEM (HRTEM), and elemental mapping images were measured to further illustrate the structure of Ni–Fe–S(5:1). Obviously, figures 2(a) and (b) depict that Ni–Fe–S(5:1) possesses the uniformly distributed nanoparticle structure featuring rich pores. The elemental mapping analysis was conducted in the selected area circled by green rectangle, and the corresponding mapping images in figures 2(c)–(f) demonstrate that the even distribution of sulfur, iron, and nickel. The ICP-AES measurement confirms that the molar ratio of nickel, iron, and sulfur in Ni–Fe–S(5:1) is determined to be 5.35:1:4.67, suggesting the sulfur-deficient structure which is favorable for exposing more metal active sites for electrocatalytic process. In addition, it can be found that O element appears on the material surface, which is attributed to the inevitable surface oxidation of the material. HRTEM images were then obtained to further illustrate the crystal structure. As observed in figure 2(g), the two lattice fringes of 0.30 and 0.27 nm are ascribed to (310) and (023) crystal plane of Ni_9S_8, respectively, and the interplanar spacing of 0.17 nm is attributed to (440) plane of $Fe_5Ni_4S_8$. The HRTEM results are consistent with XRD analysis, indicating the formation of two phases. The existence of two phases is conducive to tune the electronic structure and integrate the advantages of different phases during electrocatalytic process. Notably, as depicted by blue arrows, many defects are observed which are beneficial for regulating the electronic

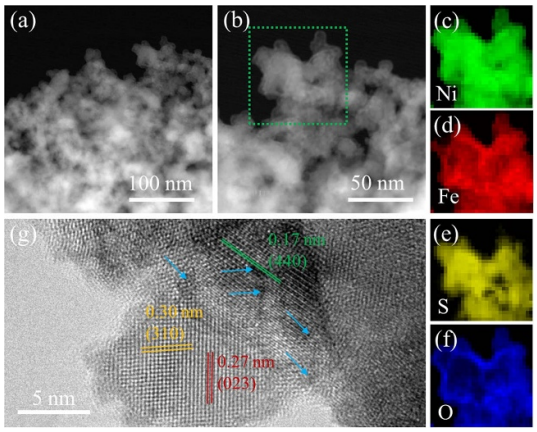

Figure 2. (a), (b) STEM and (g) HRTEM images, and elemental mappings of (c) Ni, (d) Fe, (e) S and (f) O for Ni–Fe–S(5:1).

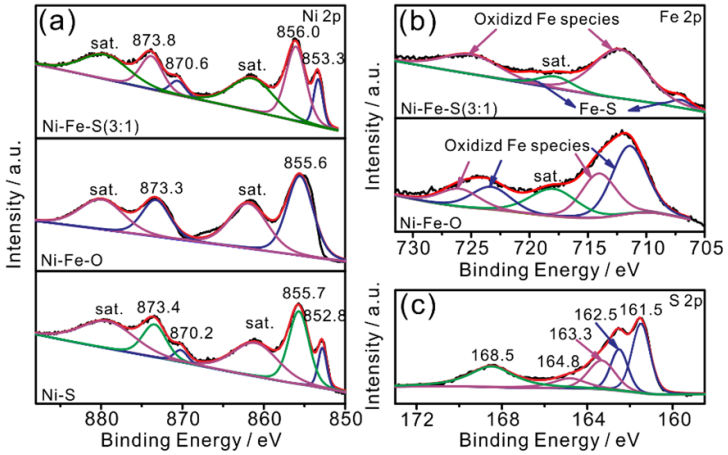

Figure 3. High resolution (a) Ni 2p and (b) Fe 2p XPS spectra for Ni–Fe–S(5:1) and contrast materials. (c) High resolution S 2p XPS spectrum for Ni–Fe–S(5:1).

structure and electron transport, optimizing the absorption energy of active species, thereby promoting the electrocatalytic activity.

The surface elemental composition and the valence state were then examined by XPS measurements. As depicted from the XPS survey spectra in figure S2, it is observed the existence of Ni, Fe, and S in Ni–Fe–S(5:1) materials, the presence of Ni, Fe, and O elements in Ni–Fe–O materials and the presence of Ni and S elements in Ni–S samples, further demonstrating the successful sulfidation with the proposed one-pot hydrothermal strategy. The high-resolution Ni 2p XPS spectra (figure 3(a)) depict that Ni–Fe–S(5:1) possesses two peaks at 853.3 and 870.6 eV attributed to nickel(II) in sulfides, and two peaks at 856.0 and 873.8 eV corresponding to oxidized nickel species along with two satellites [34–37]. For Ni–Fe–O, there are four peaks two of which at 855.6 and 873.3 eV belonging to oxidized nickel in oxides [34, 35]. For Ni–S, six peaks are observed, two of which at 852.8 and 870.2 eV belonging to nickel(II) in sulfides, and two of which at 855.7 and 873.4 eV correspond to oxidized nickel [36, 37]. Additionally, for Ni–Fe–S(5:1), five peaks appear in the high-resolution Fe 2p XPS spectra (figure 3(b)), in which peaks at 707.0 and 720.0 eV, as well as 712.3 and 725.0 eV belong to Fe–S bond, and oxidized iron species due to surface oxidation of catalysts, respectively [36, 38]. For Ni–Fe–O, four peaks at 711.5, 714.1, 723.3, and 726.0 eV are ascribed to oxidized iron [35, 39]. In the high-resolution S 2p XPS spectra of Ni–Fe–S(5:1) (figure 3(c)), peaks located at 161.5 and l62.5 eV, 163.3 and 164.8 eV correspond to metal–S bond in sulfides along with peaks at 168.5 eV belonging to sulfate originated from surface oxidation [40, 41]. For Ni–S, there are three deconvoluted peaks (figure S3), in which peaks at 161.8 and 163.3 eV correspond to Ni–S bond with the peak at 168.1 eV attributed to sulfate because of surface oxidation [42, 43]. Clearly, the absence of sulfide in Ni–Fe–O suggests that the formation of sulfide can be regulated by controlling the addition of sulfur source. Besides, the enhancement of electronic conductivity of Ni–Fe–S(5:1) in comparison with Ni–Fe–O is conducive to facilitating the electron transport during electrochemical process. Additionally, it is notable that the Ni 2p

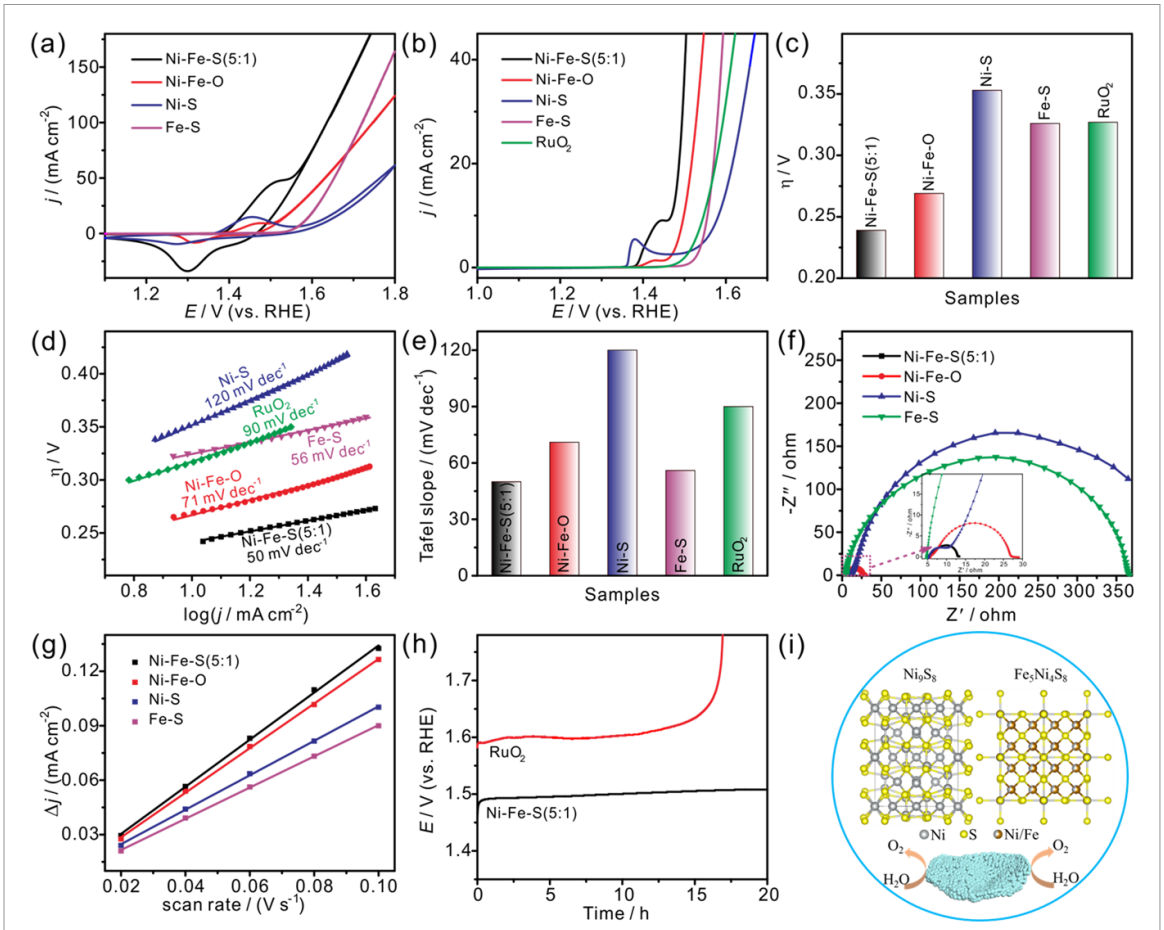

Figure 4. (a) CV curves and (b) LSV curves of Ni–Fe–S(5:1) and the contrast samples, and (c) the corresponding overpotential at 10 mA cm^{-2}, and (d), (e) Tafel slope. (f) Nyquist plots and (g) the relationship between Δj and scan rate for Ni–Fe–S(5:1), the contrast samples. (h) Chronopotentiometric curves of Ni–Fe–S(5:1) and RuO_2 via fixing the current density to 10 mA cm^{-2}. (i) Schematic representation of the OER process on Ni–Fe–S(5:1) catalysts.

XPS spectrum of Ni–Fe–S(5:1) shifts positively compared with that of Ni–S, revealing the introduction of iron could modulate the electronic structure of nickel, which may lead to the optimization of binding energy of active intermediates during the electrocatalytic reaction.

To investigate the electrochemical performances of the materials toward OER, a three-electrode setup was employed in 1.0 M KOH solution. CV measurements were conducted in the potential window between 1.1 and 1.8 V vs RHE. As depicted in figure 4(a), the Ni–S, Ni–Fe–O, and Ni–Fe–S(5:1) samples show evident redox peaks compared with Fe–S sample, attributed to the oxidation and reduction of Ni. Besides, the *in-situ* generation of metal oxo/hydroxides on the catalyst surface are considered as the OER active sites for promoting the catalytic reaction [36]. The electrocatalytic activities of the materials were then examined by LSV curves and the corresponding overpotential at a current density of 10 mA cm^{-2} (η_{10}). Figures 4(b) and (c) show the overpotential of Ni–Fe–S(5:1) is 239 mV, which is 87, 114, 30 mV lower than Fe–S, Ni–S, and Ni–Fe–O, suggesting the coexistence of iron and nickel and the better electronic conductivity than Ni–Fe–O are beneficial for the enhancement of electrocatalytic activity. Besides, the catalytic activity of Ni–Fe–S(5:1) is superior to RuO_2 and recently reported Ni and Fe based sulfides (listed in table S1), further illustrating its outstanding OER activity. Figures 4(d) and (e) depict the corresponding Tafel slope resulting from LSV curves. Apparently, the Tafel slope of Ni–Fe–S(5:1) is calculated to be 50 mV dec^{-1}, which is smaller than Ni–Fe–O (71 mV dec^{-1}), Ni–S (120 mV dec^{-1}), RuO_2 (90 mV dec^{-1}), and Fe–S (56 mV dec^{-1}), reflecting the expedited water oxidation reaction kinetics. EIS measurement was further carried out to illustrate the OER kinetics. As depicted in figure 4(f), the Nyquist plot of Fe–S, Ni–S, Ni–Fe–O, and Ni–Fe–S(5:1) all exhibits a semi-circle shape, and Ni–Fe–S(5:1) possesses the smallest charge transfer resistance among these four samples, further reflecting the fast OER kinetics. Additionally, Faradic efficiency was determined by collecting oxygen with drainage method [44, 45]. Figure S4 displays the nearly 100% Faradic efficiency of Ni–Fe–S(5:1), revealing that the observed current is generated from OER. The excellent OER activity from LSV curves and the accelerated reaction kinetics demonstrated by Tafel slope and EIS determination may be attributed to the unique heterostructured nanoparticles with two phases of Ni_9S_8 and $Fe_5Ni_4S_8$, the existence

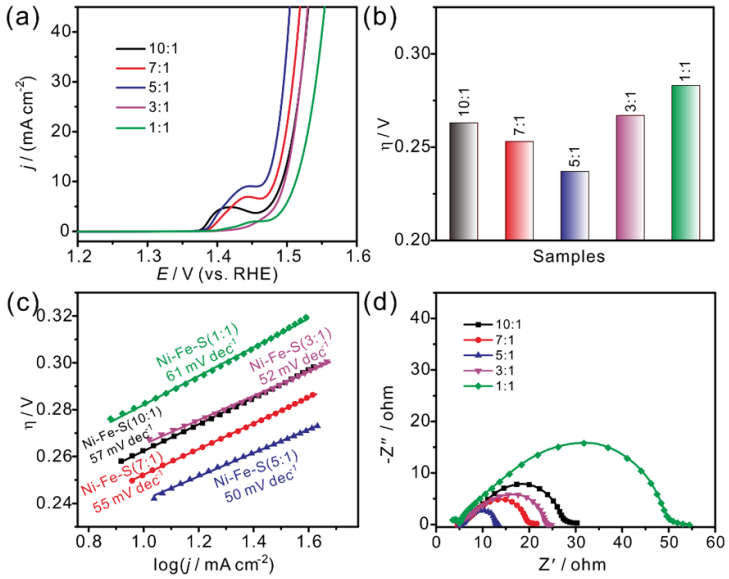

Figure 5. (a) LSV curves of Ni–Fe–S materials obtained by changing the mass ratio of nickel and iron precursors, and the corresponding (b) overpotential at the current density of 10 mA cm^{-2}, (c) Tafel slope, and (d) Nyquist plots.

of defects, as well as the porous-featured and uniformly distributed nanoparticles, favorable for optimizing the electronic structure and promoting the better utilization of active sites. In order to demonstrate the effect of electrochemical surface area (ECSA) on OER activity. CV measurements were performed under the potential window of 1.1–1.2 V vs RHE to acquire electrochemical double-layer capacitance (C_{dl}) because ECSA is proportional to C_{dl}. Obviously, Ni–Fe–S(5:1) possesses the largest ECSA, enabling catalytically active sites to be used effectively.

To study the molar ratio of Ni and Fe precursors on OER activities, different samples were synthesized by changing the molar ratio of the added nickel and iron salts to 10:1, 7:1, 5:1, 3:1, 1:1. LSV curves and the corresponding overpotential at 10 mA cm^{-2} were depicted in figure 5. It is observed that Ni–Fe–S(5:1) exhibits optimal electrocatalytic activities for OER with a lower overpotential compared with the samples prepared under other molar ratios. In addition, figures 5(c) and (d) present Ni–Fe–S(5:1) possesses the smallest Tafel slope and the lowest charge transfer resistance, further reflecting the fast kinetics during the OER process. Therefore, the molar ratio of 5:1 was chosen as the optimal condition to synthesize Ni–Fe–S materials. On the other hand, the influence of hydrothermal temperature on the catalytic activity was studied. Figure 6 depicts η_{10} of the samples obtained at 200 °C is lower than the other materials synthesized at 140, 160, 180, and 220 °C, demonstrating that the optimal OER activities can be obtained under hydrothermal treatment at the temperature of 200 °C. Besides, Tafel slope in figure 6(c) and Nyquist plot in figure 6(d) show that Ni–Fe–S(5:1) obtained at 200 °C exhibits smaller Tafel slope and charge transfer resistance, revealing the accelerated OER kinetics, which may be due to the incomplete sulfidation under lower hydrothermal temperature and the easy aggregation of nanoparticles under higher temperature.

In view of the superior electrocatalytic activity of Ni–Fe–S(5:1), its stability was studied since it is another significant criteria to examine the electrocatalytic performance of the materials. Accordingly, chronopotentiometry was conducted by fixing the current density to 10 mA cm^{-2}. For comparison, the stability of RuO_2 was also examined at the same measurement condition. Figure 4(h) displays that after continuous determination for 20 h, the potential of RuO_2 increases sharply. In contrast, the slightly increased potential of Ni–Fe–S(5:1) suggests excellent long-lasting stability, indicating the potential application in OER-related energy conversion and storage devices. Electrochemical tests demonstrate the superior electrocatalytic OER performance of Ni–Fe–S(5:1) with excellent activity and long-term stability. Combined electrochemical results with the physical characterization, the superior OER activity of Ni–Fe sulfides obtained at the molar ratio of adding Ni and Fe of 5:1 and hydrothermal temperature of 200 °C could be ascribed to the following aspects. Firstly, the obtained heterostructured nanoparticles with two phases of Ni_9S_8 and $Fe_5Ni_4S_8$ (figure 4(i)) can optimize electronic structure by effectively integrate the merits of different phases, improving the absorption energy of intermediates [46]. And the better electronic conductivity of Ni–Fe–S(5:1) in comparison with corresponding oxides can facilitate the electron transport during OER process. Besides, numerous defects generated on the catalysts can expose more active sites and modulate the electronic structure, thereby favorable for promoting the electrocatalytic OER [47].

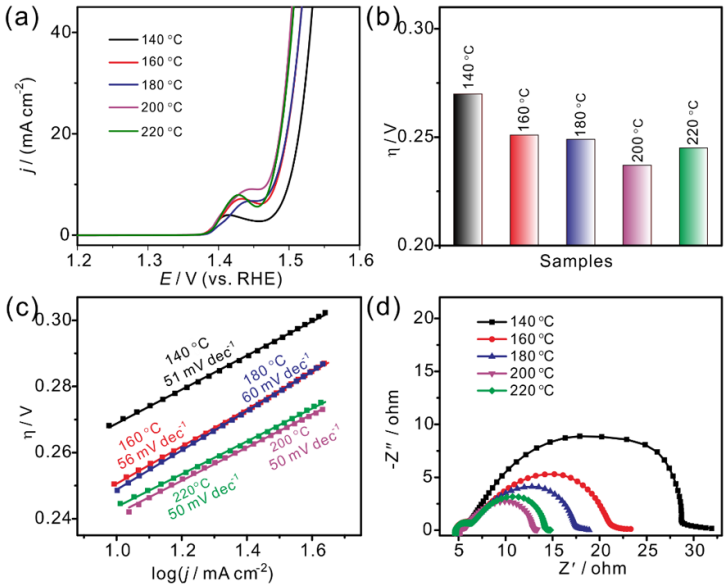

Figure 6. (a) LSV curves of Ni–Fe–S materials obtained by changing hydrothermal temperature, and the corresponding (b) overpotential at 10 mA cm^{-2}, (c) Tafel slope, and (d) Nyquist plots.

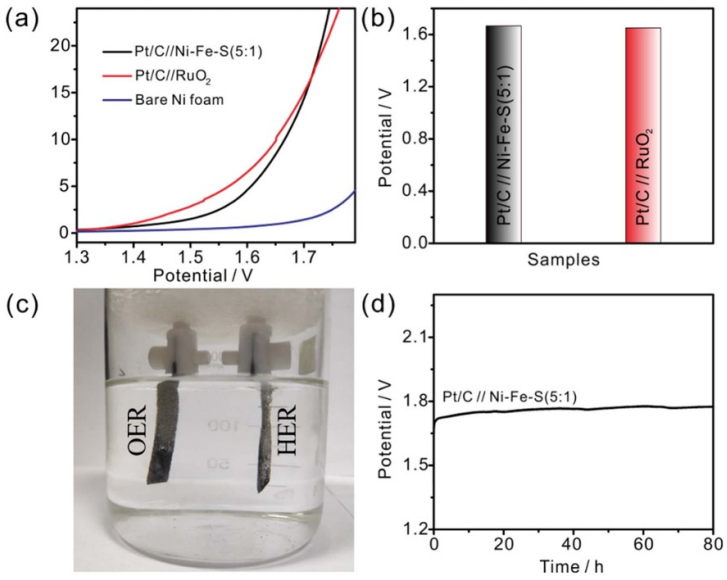

Figure 7. (a) Polarization curves of Pt/C//Ni–Fe–S(5:1), Pt/C//RuO_2, bare Ni foam for overall water splitting, and (b) the corresponding potential at 10 mA cm^{-2}. (c) Optical photograph and (d) chronopotentiometric curve of Pt/C//Ni–Fe–S(5:1) for overall water electrolysis.

Additionally, porous structure and even-distributed nanoparticles are conducive to ensuring sufficient contact between electrolyte and reactants, facilitating mass transport, and making better use of active sites [48]. The compositional and structural advantages enable Ni–Fe–S(5:1) as a promising candidate for electrocatalytic water oxidation.

Considering the superior OER performance of Ni–Fe–S(5:1), a home-made two-electrode electrolyzer was assembled to investigate the promising application in overall water splitting. The Ni–Fe–S(5:1) catalyst and Pt/C were supported on Ni foam serving as the anode and cathode, respectively, for water electrolysis. For comparison, Pt/C and RuO_2 were supported onto Ni foam as cathode and anode, respectively, since they were considered as highly active electrocatalysts for HER and OER, respectively. Besides, the electrocatalytic performance of bare Ni foam was also studied. LSV curves and the corresponding voltage for acquiring 10 mA cm^{-2} in figures 7(a) and (b) manifest that the negligible influence of Ni foam due to its inferior activity. Apparently, Ni–Fe sulfide possesses superior electrocatalytic activity for overall water splitting with a cell voltage of 1.66 V to deliver 10 mA cm^{-2}, comparable to the noble-metal-based system. Furthermore, the

stability of Ni–Fe sulfide based electrolyzer was tested by chronopotentiometry at a fixed current density of 10 mA cm^{-2}. It is clear that Ni–Fe–S(5:1) based system displays no evident potential variation compared with Pt/C//RuO_2 based system after continuous electrolysis for 80 h, revealing its promising prospect for practical application in water splitting.

4. Conclusions

In summary, an efficient defect-rich $Ni_9S_8/Fe_5Ni_4S_8$ heterostructured nanoparticles was synthesized by using a one-pot hydrothermal strategy for OER. The obtained Ni–Fe–S(5:1) catalyst possesses two phases of Ni_9S_8 and $Fe_5Ni_4S_8$, many defects and uniformly distributed nanoparticles with porous structure, which are favorable for modulating electronic structure, facilitating electron and mass transport, and making active sites to be effectively used during the electrocatalytic process. Benefiting from these unique compositional and structural merits, the as-synthesized Ni–Fe–S(5:1) exhibit enhanced electrocatalytic OER property with an overpotential of 239 mV to delivering 10 mA cm^{-2}. Moreover, in home-made two-electrode system, Ni–Fe–S(5:1) coupled Pt/C cell shows comparable electrocatalytic performance to Pt/C and RuO_2 based system for overall water splitting.

Data availability statement

The data generated and/or analyzed during the current study are not publicly available for legal/ethical reasons but are available from the corresponding author on reasonable request.

Acknowledgments

This work was supported by the Research Foundation for Distinguished Scholars of Qingdao Agricultural University (665-1120019 and 665-1119008). The authors thank the Central Laboratory of Qingdao Agriculture University for the physical characterization.

ORCID iDs

Xuyun Guo https://orcid.org/0000-0003-0365-7545
Cuijuan Xuan https://orcid.org/0000-0001-9514-5947

References

[1] Afroz K, Moniruddin M, Bakranov N, Kudaibergenov S and Nuraje N 2018 A heterojunction strategy to improve the visible light sensitive water splitting performance of photocatalytic materials *J. Mater. Chem.* A **6** 21696–718
[2] Chen S-H, Jiang Y-S and Lin H Y 2020 Easy synthesis of $BiVO_4$ for photocatalytic overall water splitting *ACS Omega* **5** 8927–33
[3] Yue Q, Sun J, Chen S, Zhou Y, Li H, Chen Y, Zhang R, Wei G and Kang Y 2020 Hierarchical mesoporous MXene–NiCoP electrocatalyst for water-splitting *ACS Appl. Mater. Interfaces* **12** 18570–7
[4] Aktar A, Ahmmed S, Hossain J and Ismail A B M 2020 Solution-processed synthesis of copper oxide (Cu_xO) thin films for efficient photocatalytic solar water splitting *ACS Omega* **5** 25125–34
[5] Huang Y *et al* 2020 The application of perovskite materials in solar water splitting *J. Semicond.* **41** 011701
[6] Li H, Zhu X, Tang Q, Wang S and Yu J 2020 Three-dimensional NiFe layered double hydroxide nanowire/nanoporous Ni/nickel foam for efficient oxygen evolution *J. Electrochem. Soc.* **167** 146513
[7] Feng C, Faheem M B, Fu J, Xiao Y and Li Y 2020 Fe-based electrocatalysts for oxygen evolution reaction: progress and perspectives *ACS Catal.* **10** 4019–47
[8] Chandrasekaran S, Ma D, Ge Y, Deng L and Zhang H 2020 Electronic structure engineering on two-dimensional (2D) electrocatalytic materials for oxygen reduction, oxygen evolution, and hydrogen evolution reactions *Nano Energy* **77** 105080
[9] Srinivas K, Chen Y, Wang B, Yu B, Wang X, Hu Y, Lu Y, Li W, Zhang W and Yang D 2020 Metal-organic framework-derived NiS/Fe_3O_4 heterostructure-decorated carbon nanotubes as highly efficient and durable electrocatalysts for oxygen evolution reaction *ACS Appl. Mater. Interfaces* **12** 31552–63
[10] Lyu F, Wang Q, Choi S M and Yin Y 2019 Noble-metal-free electrocatalysts for oxygen evolution *Small* **15** 1804201
[11] Han L, Dong S and Wang E 2016 Transition-metal (Co, Ni, and Fe)-based electrocatalysts for the water oxidation reaction *Adv. Mater.* **28** 9266–91
[12] Lu Y, Fan D, Chen Z, Xiao W, Cao C and Yang X 2020 Anchoring Co_3O_4 nanoparticles on MXene for efficient electrocatalytic oxygen evolution *Sci. Bull.* **65** 460–6
[13] Wang K, Wang X, Li Z, Yang B, Ling M, Gao X, Lu J, Shi Q, Lei L and Wu G 2020 Designing 3d dual transition metal electrocatalysts for oxygen evolution reaction in alkaline electrolyte: beyond oxides *Nano Energy* **77** 105162
[14] Mohammed-Ibrahim J 2020 A review on NiFe-based electrocatalysts for efficient alkaline oxygen evolution reaction *J. Power Sources* **448** 227375
[15] Anantharaj S, Kundu S and Noda S 2020 'The Fe effect': a review unveiling the critical roles of Fe in enhancing OER activity of Ni and Co based catalysts *Nano Energy* **80** 105514
[16] Gao R and Yan D 2020 Recent development of Ni/Fe-based micro/nanostructures toward photo/electrochemical water oxidation *Adv. Energy Mater.* **10** 1900954

[17] Xiao H, Shin H and Goddard W A 2018 Synergy between Fe and Ni in the optimal performance of (Ni, Fe)OOH catalysts for the oxygen evolution reaction *Proc. Natl Acad. Sci. USA* **115** 5872–7

[18] Sun Y, Zhang T, Li C, Xu K and Li Y 2020 Compositional engineering of sulfides, phosphides, carbides, nitrides, oxides, and hydroxides for water splitting *J. Mater. Chem.* A **8** 13415–36

[19] Peng X, Yan Y, Jin X, Huang C, Jin W, Gao B and Chu P K 2020 Recent advance and prospectives of electrocatalysts based on transition metal selenides for efficient water splitting *Nano Energy* 105234

[20] Fu G, Wang J, Chen Y, Liu Y, Tang Y, Goodenough J B and Lee J M 2018 Exploring indium-based ternary thiospinel as conceivable high-potential air-cathode for rechargeable Zn-air batteries *Adv. Energy Mater.* **8** 1802263

[21] Wu Z, Wu H, Niu T, Wang S, Fu G, Jin W and Ma T 2020 Sulfurated metal-organic frameworks derived nanocomposites for efficient bifunctional oxygen electrocatalysis and rechargeable Zn-air battery *ACS Sustain. Chem. Eng.* **8** 9226–34

[22] Zhang W, Li D, Zhang L, She X and Yang D 2019 NiFe-based nanostructures on nickel foam as highly efficiently electrocatalysts for oxygen and hydrogen evolution reactions *J. Energy Chem.* **39** 39–53

[23] Peng L, Shah S S A and Wei Z 2018 Recent developments in metal phosphide and sulfide electrocatalysts for oxygen evolution reaction *Chin. J. Catal.* **39** 1575–93

[24] Chen X, Liu Q, Bai T, Wang W, He F and Ye M 2020 Nickel and cobalt sulfide-based nanostructured materials for electrochemical energy storage devices *Chem. Eng. J.* **409** 127237

[25] Guo Y, Park T, Yi J W, Henzie J, Kim J, Wang Z, Jiang B, Bando Y, Sugahara Y and Tang J 2019 Nanoarchitectonics for transition-metal-sulfide-based electrocatalysts for water splitting *Adv. Mater.* **31** 1807134

[26] Wang H, Tang J, Li Y, Chu H, Ge Y, Baines R, Dong P, Ajayan P M, Shen J and Ye M 2018 Template-free solvothermal preparation of ternary $FeNi_2S_4$ hollow balloons as RuO_2-like efficient electrocatalysts for the oxygen evolution reaction with superior stability *J. Mater. Chem.* A **6** 19417–24

[27] Ni B, He T, Jo W, Zhang S, Ouyang C, Long Y, Zhuang J and Wang X 2018 The formation of $(NiFe)S_2$ pyrite mesocrystals as efficient pre-catalysts for water oxidation *Chem. Sci.* **9** 2762–7

[28] Cao Y, Zheng X, Zhang H, Zhang J, Han X, Zhong C, Hu W and Deng Y 2019 Interface engineering of NiS_2/CoS_2 nanohybrids as bifunctional electrocatalysts for rechargeable solid state Zn-air battery *J. Power Sources* **437** 226893

[29] Du F, Shi L, Zhang Y, Li T, Wang J, Wen G, Alsaedi A, Hayat T, Zhou Y and Zou Z 2019 Foam-like $Co_9S_8/N_{i3}S_2$ heterostructure nanowire arrays for efficient bifunctional overall water-splitting *Appl. Catal.* B **253** 246–52

[30] Wu Z, Zhao Y, Jin W, Jia B, Wang J and Ma T 2020 Recent progress of vacancy engineering for electrochemical energy conversion related applications *Adv. Funct. Mater.* **31** 2009070

[31] Liu H, Lei W, Tong Z, Li X, Wu Z, Jia Q, Zhang S and Zhang H 2020 Defect engineering of 2D materials for electrochemical energy storage *Adv. Mater. Interfaces* **7** 2000494

[32] Zhao H and Yuan Z-Y 2021 Surface/interface engineering of high-efficiency noble metal-free electrocatalysts for energy-related electrochemical reactions *J. Energy Chem.* **54** 89–104

[33] Zhu Y P, Guo C, Zheng Y and Qiao S-Z 2017 Surface and interface engineering of noble-metal-free electrocatalysts for efficient energy conversion processes *Acc. Chem. Res.* **50** 915–23

[34] Zhan Y, Lu M, Yang S, Liu Z and Lee J Y 2016 The origin of catalytic activity of nickel phosphate for oxygen evolution in alkaline solution and its further enhancement by iron substitution *ChemElectroChem* **3** 615–21

[35] Xuan C, Wang J, Xia W, Zhu J, Peng Z, Xia K, Xiao W, Xin H L and Wang D 2018 Heteroatom (P, B, or S) incorporated NiFe-based nanocubes as efficient electrocatalysts for the oxygen evolution reaction *J. Mater. Chem.* A **6** 7062–9

[36] Xuan C, Lei W, Wang J, Zhao T, Lai C, Zhu Y, Sun Y and Wang D 2019 Sea urchin-like Ni-Fe sulfide architectures as efficient electrocatalysts for the oxygen evolution reaction *J. Mater. Chem.* A **7** 12350–7

[37] Park G D, Cho J S and Kang Y C 2015 Sodium-ion storage properties of nickel sulfide hollow nanospheres/reduced graphene oxide composite powders prepared by a spray drying process and the nanoscale Kirkendall effect *Nanoscale* **7** 16781–8

[38] Jiang F, Peckler L T and Muscat A J 2015 Phase pure pyrite FeS_2 nanocubes synthesized using oleylamine as ligand, solvent, and reductant *Cryst. Growth Des.* **15** 3565–72

[39] Barforoush J M, Jantz D T, Seuferling T E, Song K R, Cummings L C and Leonard K C 2017 Microwave-assisted synthesis of a nanoamorphous $(Ni_{0.8}, Fe_{0.2})$ oxide oxygen-evolving electrocatalyst containing only 'fast' sites *J. Mater. Chem.* A **5** 11661–70

[40] Hao P, Xin Y, Tian J, Li L, Xie J, Lei F, Tong L, Liu H and Tang B 2020 Novel $(Ni, Fe)S_2/(Ni, Fe)_3S_4$ solid solution hybrid: an efficient electrocatalyst with robust oxygen-evolving performance *Sci. China Chem.* **63** 1030–9

[41] Thangasamy P, Oh S, Nam S, Randriamahazaka H and Oh I K 2020 Ferrocene-incorporated cobalt sulfide nanoarchitecture for superior oxygen evolution reaction *Small* **16** 2001665

[42] Yuan C Z, Sun Z T, Jiang Y F, Yang Z K, Jiang N, Zhao Z W, Qazi U Y, Zhang W H and Xu A W 2017 One-step *in situ* growth of iron-nickel sulfide nanosheets on FeNi alloy foils: high-performance and self-supported electrodes for water oxidation *Small* **13** 1604161

[43] Wu F, Guo X, Hao G, Hu Y and Jiang W 2019 Synthesis of iron-nickel sulfide porous nanosheets via a chemical etching/anion exchange method for efficient oxygen evolution reaction in alkaline media *Adv. Mater. Interfaces* **6** 1900788

[44] Jing S, Zhang L, Luo L, Lu J, Yin S, Shen P K and Tsiakaras P 2018 N-doped porous molybdenum carbide nanobelts as efficient catalysts for hydrogen evolution reaction *Appl. Catal.* B **224** 533–40

[45] Xu F, Qian G, Chen W, Luo L, Shen F and Yin S 2020 Copper-iron selenides ultrafine nanowires as cost-effective catalysts for the oxygen evolution reaction at large-current-density *J. Phys. Chem.* C **124** 19595–602

[46] Xu H, Shang H, Wang C, Jin L, Chen C, Wang C and Du Y 2020 Three-dimensional open $CoMoO_x/CoMoS_x/CoS_x$ nanobox electrocatalysts for efficient oxygen evolution reaction *Appl. Catal.* B **265** 118605

[47] Chen Z, Zhong H, Hu W, Yin H, Cao G, Wen H, Wang J and Wang P 2019 Highly dispersed $Ni_{2-x}Mo_xP$ nanoparticles on oxygen-defect-rich $NiMoO_{4-y}$ nanosheets as an active electrocatalyst for alkaline hydrogen evolution reaction *J. Power Sources* **444** 227311

[48] Qi J, Zhang W and Cao R 2018 Porous materials as highly efficient electrocatalysts for the oxygen evolution reaction *ChemCatChem* **10** 1206–20